

# A Bayesian Approach for Interpolating Clear-Sky MODIS Land Surface Temperatures on Areas With Extensive Missing Data

Yuhong Chen<sup>1</sup>, Zhuotong Nan<sup>1</sup>, Shuping Zhao, and Yi Xu

**Abstract**—The MODIS land surface temperature (LST) products contain large areas of missing data due to cloud contamination. Interpolating clear-sky equivalent LSTs on those areas is a first step in a stepwise approach toward fully recovering missing data. A previous study (viz. the Yu method) has implemented an effective clear-sky interpolation method, especially targeting large-area missing data. The Yu method postulates several global reference LST images that contain over 90% of valid pixels and that are assumed to have a close statistical relationship to the interpolated images. However, in practice, such reference images are rarely available throughout a one-year cycle, and the time gaps between the available reference images and the interpolated images are often huge, resulting in compromised interpolation accuracy. In this study, we intended to address those weaknesses and propose a novel clear-sky interpolation approach. The proposed approach uses multiple temporally proximate images as reference images, with which multiple initial estimates are made by an empirically orthogonal function method and then fused by a Bayesian approach to achieve a best estimate. The proposed approach was compared through two experiments to the Yu method and two other widely used methods, i.e., harmonic analysis of time series and co-kriging. Both experiments demonstrate the superiority of the proposed approach over those established methods, as evidenced by higher spatial correlation coefficients (0.90–0.94) and lower root-mean-square errors (1.19–3.64 °C) it achieved when measured against the original data that were intentionally removed.

**Index Terms**—Bayesian approach, data fusion, data interpolation, empirical orthogonal function (EOF), land surface temperature (LST), similarity theory.

## I. INTRODUCTION

**L**AND surface temperature (LST) is a key variable for monitoring surface energy budget, determined by the land

surface–atmosphere interactions and the energy fluxes between the atmosphere and the ground. It is widely used in a variety of studies including climate change, hydrological cycle, vegetation monitoring, and ecosystem assessment [1]–[3]. The LST products from the moderate resolution imaging spectroradiometer (MODIS) onboard the Terra and Aqua satellites have become one of the most commonly used LST products due to their high spatial and temporal resolutions [4], [5]. However, the MODIS LST products contain a large portion of missing data as a result of cloud contamination, high aerosol content, sensor failure, and quality control. On average, approximately 35% of the global surface is obscured by clouds at any one time [6]. The average cloud coverage amounts to more than 50% on the Qinghai-Tibet Plateau (QTP) [7], [8].

Many techniques have been developed to fill up missing values in the MODIS LST products, such as combining microwave data [9]–[12], deriving missing data from the surface energy balance (SEB) equation [13]–[15], and adopting stepwise strategies [16]–[20]. Microwave methods take advantage of microwave measurements under cloudy conditions, but are generally limited by the coarse resolution of passive microwave data and the large uncertainties associated with the data that are induced by the interference of inhomogeneous underlying surface conditions [21], [22]. The SEB methods are physically explicit, but their applicability is highly dependent on the availability of meteorological observations, such as air temperature, specific humidity, and wind speed [15]. Stepwise approaches have been developed in recent years to ease the mission in a way, breaking the full process into separate steps: 1) estimating clear-sky equivalent LST values assuming no cloud effects on the missing pixels and 2) imposing cloud-effects on those equivalent LSTs on the cloud obscured pixels. As such, the tasks become more specific to tackle the challenges met in each step. For example, Zhang *et al.* [16] estimated clear-sky LSTs from a diurnal evolution of LST model and recovered cloud-affected values by assuming that cloud effects can be approximated by the differences in net shortwave solar radiation and thermal inertia. Yu *et al.* [18] developed a two-step method in which clear-sky LSTs were estimated following the similarity theory and then corrected for the cloud-covered pixels considering surface energy balance. Zeng *et al.* [17] first used a multitemporal interpolation method to compute clear-sky LST values, and then in the next step, corrected for cloud effects based on a surface energy balance approach. In the work of Yang *et al.* [20], the harmonic analysis

Manuscript received August 26, 2020; revised October 11, 2020; accepted November 11, 2020. Date of publication November 16, 2020; date of current version January 6, 2021. This work was supported in part by the National Natural Science Foundation of China under Grant 41671055, Grant 41931180, and Grant 41971074, and in part by the Natural Science Program of Jiangsu Higher Education Institutions under Grant 17KJA170003. (Corresponding author: Zhuotong Nan.)

Yuhong Chen and Shuping Zhao are with the Key Laboratory of Ministry of Education on Virtual Geographic Environment, Nanjing Normal University, Nanjing 210023, China (e-mail: 171302056@stu.njnu.edu.cn; shuping@njnu.edu.cn).

Zhuotong Nan is with the Key Laboratory of Ministry of Education on Virtual Geographic Environment, Nanjing Normal University, Nanjing 210023, China, and also with the Jiangsu Center for Collaborative Innovation in Geographical Information Resource Development and Application, Nanjing 210023, China (e-mail: nanzt@njnu.edu.cn).

Yi Xu is with the Fujian Provincial Investigation, Design and Research Institute of Water Conservancy and Hydropower, Fuzhou 350001, China (e-mail: yixu1102@gmail.com).

Digital Object Identifier 10.1109/JSTARS.2020.3038188

of time series (HANTS) algorithm and Poisson image editing method were used to solve clear-sky LST values, and the cloud effects were accounted using a revised neighboring-pixel approach. The final accuracy depends on both the performance of interpolating clear-sky equivalent LSTs in the first step and bias removal of cloud effects in the next correction steps. Therefore, it is crucial to accurately interpolate clear-sky equivalent LSTs for the cloud-affected pixels in any stepwise approach toward fully recovering the missing data.

In addition, interpolating clear-sky LSTs can be meaningful in recovering nighttime missing LSTs. Unlike daytime, the cloud effects on the LSTs during nighttime are marginal since there are no incoming solar radiations at night [18]. Therefore, interpolated clear-sky LSTs can be accepted as being accurate under nighttime cloud conditions. Despite that clear-sky equivalent LSTs may differ in value from real cloudy-sky LSTs, they also have the potential to provide broadly consistent spatial and temporal patterns of LST [23], [24], and they can be useful in some applications, such as mapping permafrost [25], [26], drought monitoring [27], numerical weather prediction [28], and urban heat islands [29], where high accuracies of LST are often not demanding.

In previous studies, many methods have been developed for interpolating clear-sky LSTs assuming no cloud effects. They can be roughly classified into three categories—spatial interpolation methods [30], [31], temporal interpolation methods [32]–[35], and spatiotemporal interpolation methods [7], [36], [37]. The first category methods spatially interpolate the missing LST data using geostatistical methods and regression methods, such as inverse distance weighting (IDW) [38], regression kriging (RK) [39], and co-kriging (CoK) [40]. In this category, the predictor variables are critical to obtaining satisfactory accuracies, such as using digital elevation model (DEM) [31] and normalized differential vegetation index (NDVI) [41]. The second category methods rely on mathematical fitting to temporal LST variations. A commonly used method is to extract the missing MODIS LST values from an established diurnal temperature cycle curve [42], [43]. HANTS is also an often-used method falling within this category [33], [44]. However, the first and second categories usually lack for effectiveness in the face of large-area missing data. Spatial interpolation methods rely on the information from spatially neighboring pixels. Their performance greatly weakens when severe data losses are present in the neighborhood. For temporal interpolation methods, narrow time gaps between two available values are very important for interpolation accuracy. Unfortunately, the absence of LST observations on the QTP frequently continues for a long period, severely degrading its performance.

The third category methods maximize the use of both spatial and temporal neighborhood information and are theoretically more suitable in interpolating large-area missing data. Yu *et al.* [7] developed a viable approach for infilling massive data voids on the QTP. The Yu method is based on a similarity concept, assuming that each interpolated pixel is linked to a corresponding similar pixel set in space, in which all members have valid LST values and share high similarities with the interpolated pixel in terms of temperature change over two MODIS overpass times. When a similar pixel set is identified for an interpolated pixel,

a linear statistical relationship can be inferred using the LST values on the similar pixels that are known on both the interpolated and the reference image. The relationship is then used for interpolating the missing value on the interpolated image when the corresponding LST value on the reference image is known. The experimental applications to the QTP indicate that the Yu method outperformed conventional geostatistical methods when dealing with large-area missing data. Nevertheless, it postulates the existence of a certain number of global reference images, which should possess a high fraction (e.g., >90%) of valid pixels and a statistically close relation to the interpolated image. Unfortunately, such global reference images are rarely available in a one-year cycle on the QTP, and even if available, there are often long intervals between the qualified reference images and the interpolated image. The long intervals weaken the statistical ties between the interpolated image and the reference images and consequently, lower the interpolation accuracy. In practice, similar pixels as defined in the Yu method will have the highest similarity over two temporally proximate LST images in terms of temperature change. Proximate images thus could be ideal reference image candidates. But when using proximate images as reference images, the first obstacle is that for many interpolated pixels, the corresponding LST values remain unavailable on the proximate images as long as clouds are present, while as being qualified reference images, they should be known. As such, it is almost impossible to find a valid reference image from proximate images where all interpolated pixels are known. In addition, there are chances for abrupt temperature changes to occur between the view times of the proximate image and the interpolated image. Thus, the use of a single proximate image as a reference image would risk losing interpolation quality. A possible solution to deal with those obstacles is to use multiple proximate images preceding and succeeding the interpolated image, instead of a single one, as reference images.

In the present work, we extended the previous work of Yu *et al.* [7] by using multiple proximate images as reference images and introducing a Bayesian approach to fuse initially estimated values as a best estimate for the clear-sky equivalent LST.

## II. METHOD

### A. Proposed Approach

The proposed approach extends the methodology developed by Yu *et al.* [7], basing the same similarity concept. It assumes that each interpolated pixel has a corresponding similar pixel set in space, in which all set members share high similarities with the interpolated pixel in terms of temperature change over time. A reference image is defined as the image where the interpolated pixel and similar pixels have known LST observations. The similar pixel set can be created by measuring all known pixels on both the interpolated and the reference images and removing the pixels unsatisfying certain similarity criteria. The members of the similar pixel set are thus known on both the interpolated image and the reference image. A statistical relationship can be inferred from pairs of known LSTs of the similar pixels on both images and then applied to estimate the unknown LST of the interpolated pixel on the interpolated image.

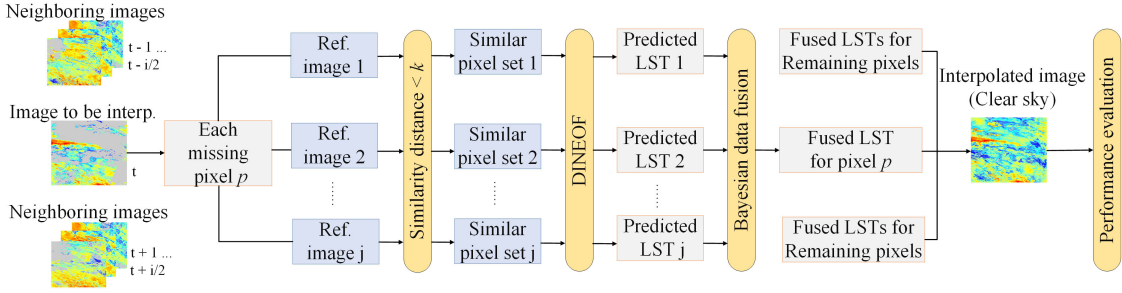


Fig. 1. Approach framework for interpolating large-area missing LST data.  $t$ : day number of an interpolated image;  $i$ : the number of candidate neighboring images;  $j$ : the number of qualified reference images (Ref. image);  $p$ : the interpolated pixel;  $k$ : a threshold of property distance, less than which the pixels measured will be selected as similar pixels for the pixel  $p$ . DINEOF: data interpolating empirical orthogonal function.

The improvements of this approach over the Yu method lie on two aspects: 1) rather than seeking universal reference images where all interpolated pixels are known, which is hard to be satisfied, as implemented in the original Yu method, we use temporally neighboring images as reference images for each interpolated pixel. Several images proximate to the interpolated image that have an adequate number of similar pixels are identified as reference images for the interpolated pixel and 2) with those proximate reference images, multiple estimates are thus made for the unknown LST of the interpolated pixel. A best estimate is then achieved through a Bayesian fusion approach so as to improve the interpolation accuracy as well as to minimize the effects of occurrence of abrupt temperature changes on the reference images.

The workflow comprises the following four steps (see Fig. 1).

- 1) Determining reference images and similar pixel sets.
- 2) Initially interpolating missing LST values using the data interpolating empirical orthogonal function (DINEOF) method.
- 3) Obtaining best estimates by a Bayesian data fusion approach.
- 4) Iterating steps 1)–3) for all pixels to be interpolated and evaluating the performance.

#### 1) Determining Reference Images and Similar Pixel Sets:

For each pixel to be interpolated, the images proximate in time to the interpolated image are checked and they can be determined as reference images if two criteria are met. First, the candidate image has a valid LST value on the interpolated pixel; and second, the candidate image holds a relatively high proportion of valid pixels. Multiple proximate reference images can be identified for each interpolated pixel by searching through a short time window (e.g., 15 days) centered on the interpolated image. The pixels to be interpolated may have different combinations of reference images.

To determine the similar pixels to the interpolated pixel, primary factors controlling the characteristics of temperature change over time are first singled out. We choose terrain factors (DEM, slope, and aspect), vegetation indices (NDVI), and thermal condition factors (solar radiation and LST) as attributes to evaluate the similarities between the interpolated pixel and the remaining pixels. Solar radiation is ignored when processing nighttime images. The simple Euclidean distance equation is prescribed as the similarity function. All pixels with known LST

values on both the reference image and the interpolated image are measured in terms of similarity and ranked in ascending order of similarity distance. The pixels with the highest similarities (similarity distance  $< k$ ) constitute a similar pixel set for this interpolated pixel (1). Because an interpolated pixel can be associated with multiple reference images, we can create multiple similar pixel sets for a single interpolated pixel corresponding to the reference images

$$P = \min (g(S^p, S^I)) \quad (1)$$

where  $P$  is the similar pixel set;  $g$  is the Euclidean distance equation;  $S^p$  and  $S^I$  denote all attributes of the pixel  $p$  and the remaining valid pixels  $I$ , respectively.

2) *Initially Interpolating Missing LST Values Using the DINEOF Method:* The DINEOF method decomposes a matrix containing spatial data into a set of empirical orthogonal functions (EOFs). The most dominant EOFs are later used to create a new matrix, which contains an estimate for the missing value [45]. We use the DINEOF method to make initial estimates for each interpolated pixel. A similarity matrix is composed of the paired LST values of the similar pixels and the interpolated pixel from both the interpolated image and the reference image. The singular value decomposition (SVD) technique, as expressed in the following, is adopted to compute EOFs of the similarity matrix [46]:

$$M = USV^T \quad (2)$$

where  $M$  is the similarity matrix, with a dimension of  $m$  rows by  $n$  columns;  $U$  and  $V$  are matrices representing spatial EOFs ( $m \times r$ ;  $r \leq \min(m, n)$ ) and temporal EOFs ( $n \times r$ ), respectively;  $S$  is a diagonal matrix ( $r \times r$ ) whose elements are the singular values of the original matrix. The importance of EOFs is determined by the corresponding singular values.

For each similar pixel set corresponding to each associated reference image, the following DINEOF steps are performed to obtain an initial estimate of the missing LST value.

a) *Constructing a similarity matrix:* Given a similar pixel set  $P$  associated with an interpolated pixel  $p$ , the corresponding similarity matrix ( $M$ ) holds the paired LST values of both  $p$  and all members of  $P$  from the interpolated and reference images, with a dimension of  $m \times 2$ . The number of rows ( $m$ ) is equal to the length of  $P$  plus one. Two columns represent the LST values on the interpolated image and the one for the reference image,



respectively. The unknown LST of  $p$  on the interpolated image is initialized to zero.

*b) Computing and decomposing residual matrix:* The residual matrix  $R$  is computed by removing the columnwise means from all elements of the similarity matrix except the unknown element. Then, the SVD is applied to decompose the residual matrix. As a result, the spatial EOFs ( $U$ ), temporal EOFs ( $V$ ), and the singular matrix ( $S$ ) are generated.

*c) Estimating the unknown value:* The most dominant spatial and temporal EOFs from the residual matrix are used in this study to rebuild a new residual matrix  $R'$ . A new similarity matrix  $M'$  is then reconstructed by adding the means back to the columns of  $R'$ . The initial estimate of  $p$  can be found at  $M'(1, 1)$ .

*3) Obtaining Best Estimates by a Bayesian Data Fusion Approach:* The DINEOF method computes multiple initial estimates of LST for a single interpolated pixel corresponding to its associated similar pixel sets. A Bayesian data fusion approach [47] is used to find a best estimate for the interpolated pixel by fusing those multiple initial estimates. The prior probability distribution of the belief is first defined and the initial estimates are used as observations to determine the likelihood function. A posterior conditional probability density function of the current state, given all previous observations, is calculated following Bayes' theorem. The best estimate is then obtained through a maximum *a posteriori* (MAP) method. We assume that  $X$  is an unknown state variable, and  $X$  obeys a prior distribution of a known form  $f_x(x)$ . The observations, denoted by  $Z_j$  are described by a likelihood function  $f_{z_j|x}(z_j|x)$ . The posterior distribution  $f_{x|z_j}(x|z_j)$  of  $X$  can be calculated by

$$f_{x|z_j}(x|z_j) = \frac{f_x(x) f_{z_j|x}(z_j|x)}{\int f_x(x') f_{z_j|x}(z_j|x') dx'} \quad (3)$$

The MAP is used for inference. It selects a value  $\hat{X}_{MAP}$  within the range of the possible values of  $X$  so that the posterior distribution is maximized (4). When there are multiple observations  $Z_j = \{z_1, z_2, \dots, z_j\}$ , the posterior distribution (3) can be written as (5) in the following:

$$\hat{X}_{MAP} = \arg \max (f_{x|z_j}(x|z_j)) \propto f_x(x) f_{z_j|x}(z_j|x) \quad (4)$$

$$\begin{aligned} & f_{x|z_j}(x|z_1, z_2 \dots z_j) \\ &= \frac{f_x(x) f_{z_1|x}(z_1|x) f_{z_2|x}(z_2|x) \dots f_{z_j|x}(z_j|x)}{\int f_x(x') f_{z_1|x}(z_1|x') f_{z_2|x}(z_2|x') \dots f_{z_j|x}(z_j|x') dx'} \end{aligned} \quad (5)$$

Assume  $j$  initial estimates have been made in response to  $j$  similar pixel sets (see Fig. 1). When  $j > 2$ , the  $j$  initial estimates are fused by the Bayesian approach to achieve a best estimate as the final interpolated value. Otherwise, the final interpolated value is assigned with the unique initial estimate ( $j = 1$ ) or as null ( $j = 0$ ). Let  $X$  be the unknown true on the interpolated pixel and  $j$  initial estimates be the observations. For all interpolated pixels, the following steps are repeated to obtain best estimates.

*a) Identifying the prior distribution:* The members of the similar pixel set share characteristics of temperature change similar to the interpolated pixel. Therefore, the LST values of those similar pixels from all  $j$  sets on the interpolated image

can be used to describe the prior distribution of the unknown  $X$  following a Gaussian distribution

$$f_x(x) = \frac{1}{\sigma_0 \sqrt{2\pi}} e^{\left\{ \frac{-(x-z_0)^2}{2\sigma_0^2} \right\}} \quad (6)$$

where  $z_0$  represents the mean and the center of the Gaussian distribution and  $\sigma_0^2$  is the variance.  $z_0$  and  $\sigma_0^2$  can be estimated by the known LST values from all similar pixels of  $j$  sets on the interpolated image.

*b) Determining the likelihood function:* The  $j$  estimates by the DINEOF method carry varying degrees of uncertainties. Each initial estimate  $z_j$  assumingly corresponds to a Gaussian distribution and is centered in the distribution [47] (7). Since  $z_j$  is estimated by a process of decomposing and reconstructing a similarity matrix through the DINEOF method, the loss of accuracy in this process can be used to measure the uncertainty associated with  $z_j$ , denoted as the variance  $\sigma_j^2$ . We measure the differences of the similarity matrix before and after the reconstruction. The variance  $\sigma_j^2$  is determined by the differences occurring in the column that represents the reference image

$$f_{z_j|x}(z_j|x) = \frac{1}{\sigma_j \sqrt{2\pi}} e^{\left\{ \frac{-(x-z_j)^2}{2\sigma_j^2} \right\}} \quad (7)$$

*c) Calculating the posterior function and the best estimate using MAP:* Bayes' theorem is used to calculate the posterior distribution of the unknown LST on  $p$  (5). The posterior distribution for multiple observations can be rewritten as (8)–(10). The MAP is then employed to obtain the maximum of the posterior distribution (11) and the best estimate of the unknown LST is given by (12) in the following:

$$f_{x|z_j}(x|z_0, z_1 \dots z_j) = \left( c \cdot \exp \left\{ - \sum_{i=0}^j \frac{(x-z_i)^2}{2\sigma_i^2} \right\} \right) / d \quad (8)$$

$$c = \frac{1}{\prod_{i=0}^j (\sqrt{2\pi}\sigma_i)} \quad (9)$$

$$d = \int \left( c \cdot \exp \left\{ - \sum_{i=0}^j \frac{(x'-z_i)^2}{2\sigma_i^2} \right\} \right) dx' \quad (10)$$

$$\hat{X}_{MAP} = \arg \max \left( c \cdot \exp \left\{ - \sum_{i=0}^j \frac{(x-z_i)^2}{2\sigma_i^2} \right\} \right) \quad (11)$$

$$\hat{X}_{MAP} = \frac{\sum_{i=0}^j x_i / \sigma_i^2}{\sum_{i=0}^j 1 / \sigma_i^2} \quad (12)$$

## B. Performance Evaluation

*1) Study Area and Data:* We chose the Qinghai-Tibet Plateau (QTP) as the study region to evaluate the proposed approach. The plateau is bounded with  $26^\circ 00' \sim 39^\circ 47' N$  and  $73^\circ 19' \sim 104^\circ 47' E$ , with an area of over 2.6 million  $\text{km}^2$ . It is the highest plateau in the world, with an average elevation of over 4000 m above sea level and has attracted increasing research interests worldwide, especially in the context of climate change [48], [49]. MODIS LST products, as an important data



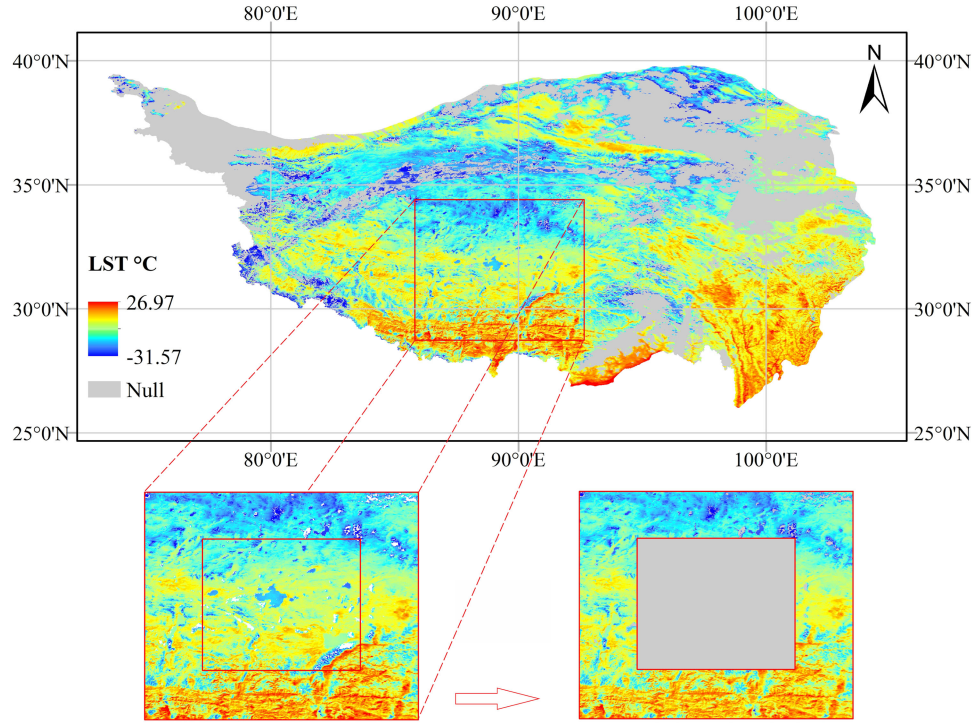


Fig. 2. Schematic procedure on fabricating data voids for the second experiment. The interpolation methods can be evaluated by comparing the interpolation results against the original values prior to removal.

source for QTP research, suffer severe data losses on the QTP due to cloud cover [7], making the QTP an ideal place to test interpolation methods. The experimental LST data are the MODIS/Terra MOD11A1 product at a 1-km spatial resolution. The Terra satellite crosses the equator at 10:30 and 22:30 local time per day. The MOD13A2 NDVI product (16 days and 1 km) from Terra was used to represent the vegetation conditions. DEM was obtained from the Shuttle Radar Topography Mission (90 m) and then, bilinearly resampled to 1 km to match the MODIS LST data. The terrain features such as slope and aspect were derived from the DEM. Clear-sky solar radiation was simply estimated from the incident angle, which depends on the time of year, latitude, elevation, slope, and aspect, plus diffuse and reflected radiation [50].

2) *Experiment Design*: Two experiments were designed to evaluate the proposed approach. One experiment aims to test the performance with real data voids that occurred on the QTP. The real data voids are results of cloud contamination, differing from clear-sky equivalent LSTs. Hence, we focused on visual inspection of spatial patterns and checked how interpolation methods work in real applications. The other tests the performance with fabricated data voids, in which the values before removal are regarded as “truth” and those clear-sky interpolation methods can be exhaustively tested for performance. In the first experiment, we selected the same two LST images as used in the literature [7] for the convenience of comparing with the Yu method (i.e., the daytime image of the tenth day and the nighttime image of the 183rd day of 2005, representing two typical cases in cold and warm seasons, respectively). The fractions of missing data in the two images are 56% and 73%, respectively. In the second

experiment, we first excluded the MODIS/Terra LST images in 2010 that are in severe loss of data (i.e., the fraction of invalid pixels  $> 80\%$ ), and then, randomly selected several images from the rest to represent different seasonal conditions and different overpass timings. A consistent patch that has minimal loss of LST observations was identified from these images as an experimental area, which covers an area of approximately  $0.56 \times 10^6 \text{ km}^2$ . The images arbitrarily selected in 2010 consist of the daytime images of the 9th, 142nd, and 255th days and the nighttime images of the 9th, 141st, and 255th days. In the identified patches on those images, one-third of the total area was removed to create artificial data holes, as illustrated in Fig. 2. Since the true LST values are known in the hollow areas, the performance of the methods can be assessed against the true values. The reference images used in the two experiments are listed in Table I. The proximate reference images may vary by interpolated pixel, so only the most frequently used reference images are listed. The global reference images for the Yu method in the first experiment were identical to the ones in the literature [7], and in the second experiment, they were identified following the exact same rules recommended in the literature [7].

We selected some representative interpolation methods for comparison with the proposed approach. Included are a spatiotemporal method—the Yu method; a temporal method—HANTS; and a spatial method—CoK. The HANTS algorithm was originally proposed for smoothing and gap-filling vegetation index (NDVI) images, and has been widely used to interpolate missing values in the LST products [32], [33]. It applies a least squares curve fitting procedure based on harmonic components. To perform HANTS, five parameters should be

TABLE I  
REFERENCE IMAGES ASSOCIATED WITH THE INTERPOLATED IMAGES FOR THE PROPOSED APPROACH AND THE YU METHOD USED IN THE TWO EXPERIMENTS

Year	Interp. image	Ref. image for the proposed approach	Ref. image for the Yu method
2005	10 <sup>th</sup> /nighttime	8 <sup>th</sup> , 12 <sup>th</sup> , 13 <sup>th</sup> , 20 <sup>th</sup> , 21 <sup>st</sup> , 24 <sup>th</sup> /nighttime	250 <sup>th</sup> /nighttime
	183 <sup>rd</sup> /daytime	177 <sup>th</sup> , 178 <sup>th</sup> , 179 <sup>th</sup> , 180 <sup>th</sup> , 189 <sup>th</sup> /daytime	251 <sup>st</sup> /daytime
2010	9 <sup>th</sup> /daytime	3 <sup>rd</sup> , 4 <sup>th</sup> , 5 <sup>th</sup> , 6 <sup>th</sup> /daytime	52 <sup>nd</sup> /daytime
	9 <sup>th</sup> /nighttime	7 <sup>th</sup> , 8 <sup>th</sup> , 10 <sup>th</sup> , 11 <sup>th</sup> /nighttime	52 <sup>nd</sup> /nighttime
	141 <sup>st</sup> /nighttime	139 <sup>th</sup> , 142 <sup>nd</sup> , 146 <sup>th</sup> , 147 <sup>th</sup> /nighttime	212 <sup>th</sup> /nighttime
	142 <sup>nd</sup> /daytime	137 <sup>th</sup> , 143 <sup>rd</sup> , 148 <sup>th</sup> /daytime	212 <sup>th</sup> /daytime
	255 <sup>th</sup> /daytime	250 <sup>th</sup> , 253 <sup>rd</sup> , 254 <sup>th</sup> , 261 <sup>st</sup> /daytime	363 <sup>rd</sup> /daytime
	255 <sup>th</sup> /nighttime	251 <sup>st</sup> , 252 <sup>nd</sup> , 253 <sup>rd</sup> , 254 <sup>th</sup> /nighttime	330 <sup>th</sup> /nighttime

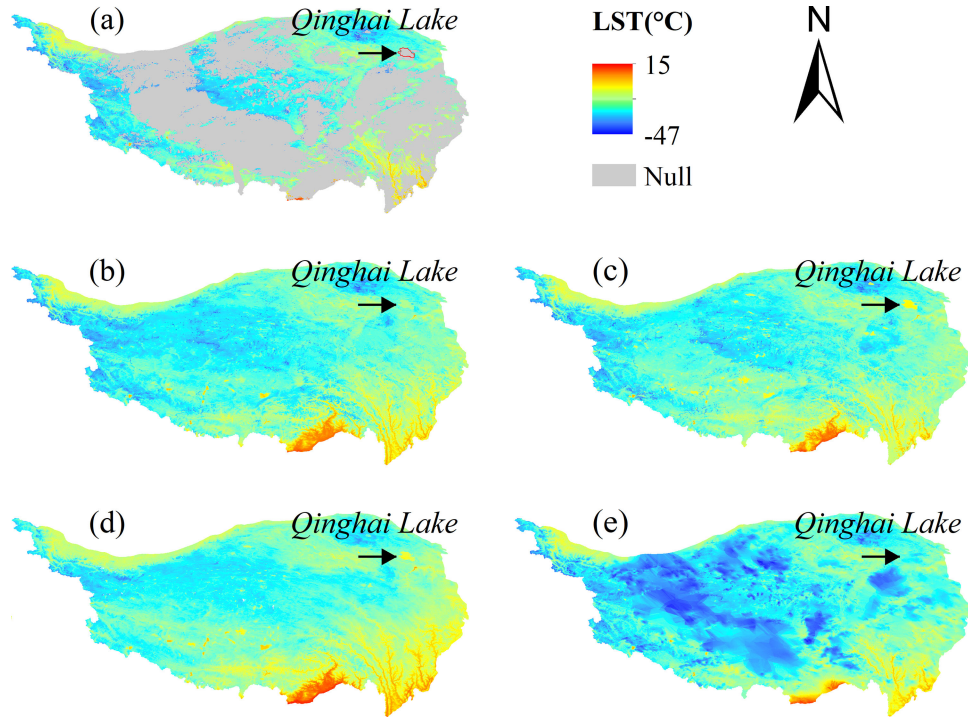


Fig. 3. Interpolated Terra/LST nighttime images for the tenth day of 2005 on the QTP using different methods. (a) Original image, (b) the proposed approach, (c) the Yu method, (d) harmonic analysis of time series (HANTS), and (e) co-Kriging (CoK) with the DEM as its covariate. The Qinghai Lake boundaries are marked on (a). The valid portions on (d) are modified due to the algorithm of HANTS.

set—the number of frequency (NOF), the high/low suppression flag (SF), the valid data range, the fit error tolerance (FET), and the degree of overdeterminedness (DOD) [51]. In this study, HANTS was applied to the LST values on each pixel on an annual basis, and the daytime and nighttime images were fitted separately. NOF was set to two, referring to the literature [33]. SF was set low because the cloud cover tends to lower the LST. The valid data range was  $-60$  to  $70^{\circ}\text{C}$ . FFT and DOD were set to 5 and  $12^{\circ}\text{C}$ , respectively. In the previous literature [7], several often-used geostatistical methods, including IDW, OK, and regression kriging, have been tested incompetent in interpolating the large-area missing data. We instead chose CoK as a representative of geostatistical methods, with DEM as its covariate in wake of its importance in controlling the temperature on the QTP. The evaluation metrics include spatial correlation (SR) (13), root-mean-square error (RMSE) (14),

mean absolute error (MAE) (15), and bias (16), given as follows:

$$\text{SR} = \frac{\sum_{i=1}^n (LST_i - \overline{LST_i}) (LST_r - \overline{LST_r})}{\sqrt{\sum_{i=1}^n (LST_i - \overline{LST_i})^2} \sqrt{\sum_{i=1}^n (LST_r - \overline{LST_r})^2}} \quad (13)$$

$$\text{RMSE} = \sqrt{\frac{1}{n} \sum_{i=1}^n (LST_i - LST_r)^2} \quad (14)$$

$$\text{MAE} = \frac{1}{n} \sum_{i=1}^n |(LST_i - LST_r)| \quad (15)$$

$$\text{Bias} = \frac{1}{n} \sum_{i=1}^n (LST_i - LST_r) \quad (16)$$

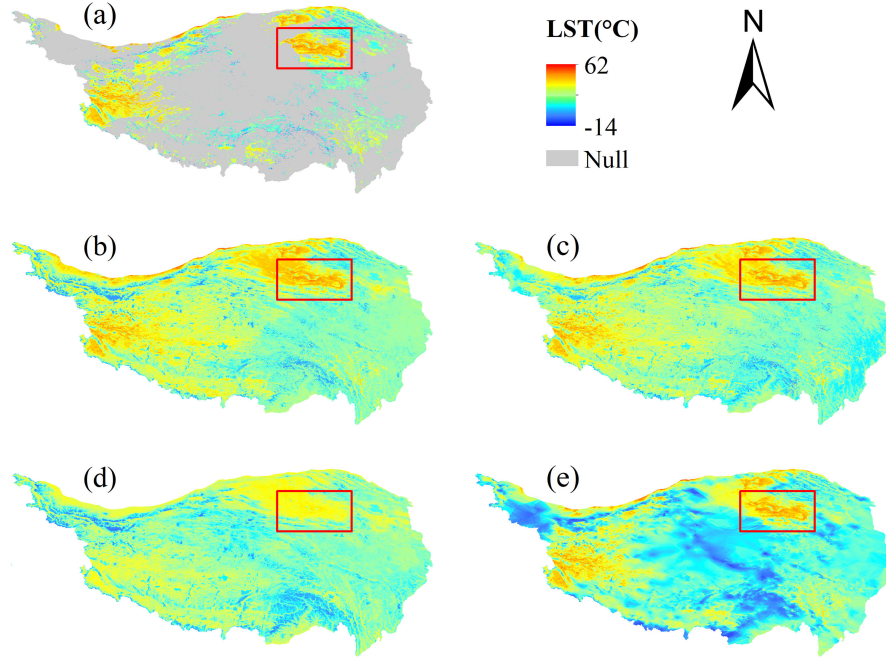


Fig. 4. Interpolated Terra/LST daytime images for the 183rd day of 2005 on the QTP using different methods. (a) Original image, (b) the proposed approach, (c) the Yu method, (d) HANTS, (e) CoK. Rectangle envelops partial Qaidam basin. The valid portions on (d) are modified due to the algorithm of HANTS.

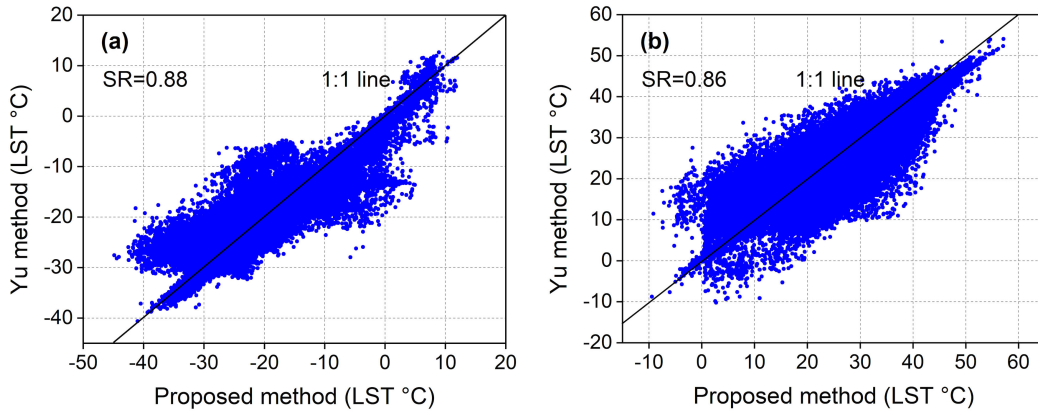


Fig. 5. Comparison of the results of the proposed approach and the Yu method on 100,000 randomly selected invalid pixels from the Terra/LST images of the (a) tenth nighttime and (b) 183rd daytime of 2005 on the QTP. The solid line indicates a 1:1 line.

where  $n$  is the number of interpolated pixels;  $LST_i$  and  $LST_r$  are the interpolated and the preremoval LST values, respectively.  $\overline{LST_i}$  and  $\overline{LST_r}$  indicate their means.

### III. RESULTS AND DISCUSSION

#### A. Performance for the Real Data Void Case

Figs. 3 and 4 show the interpolation results of a representative nighttime LST image (10th night) and a representative daytime LST image (183rd day) in 2005 on QTP, respectively, produced by the proposed approach, the Yu method, HANTS, and CoK. CoK results [see Figs. 3(e) and 4(e)] exhibit many strange patterns, especially in the northwest and southern QTP on the nighttime image and in the central zone of QTP on the daytime image. Those artifacts expose a critical weakness in CoK, as shown with

the QTP examples, for interpolating extensive missing data even if the DEM is used as a covariant. This can be explained by the fact that the CoK inherently depends on the information from spatially neighboring pixels, which are unfortunately severely lost in the case of large-area missing data. The use of DEM as covariant cannot eliminate this inherent weakness. Together with the tests demonstrated in the previous study [7], it can be reasonably concluded that conventional geostatistical methods are usually not applicable to the situation facing extensive data losses.

The results of the proposed approach [see Figs. 3(b) and 4(b)], the Yu method [see Figs. 3(c) and 4(c)], and HANTS [see Figs. 3(d) and 4(d)] appear much better in terms of spatial pattern and textural transition than the CoK. The three methods can well capture some unique temperature patterns on the QTP. The



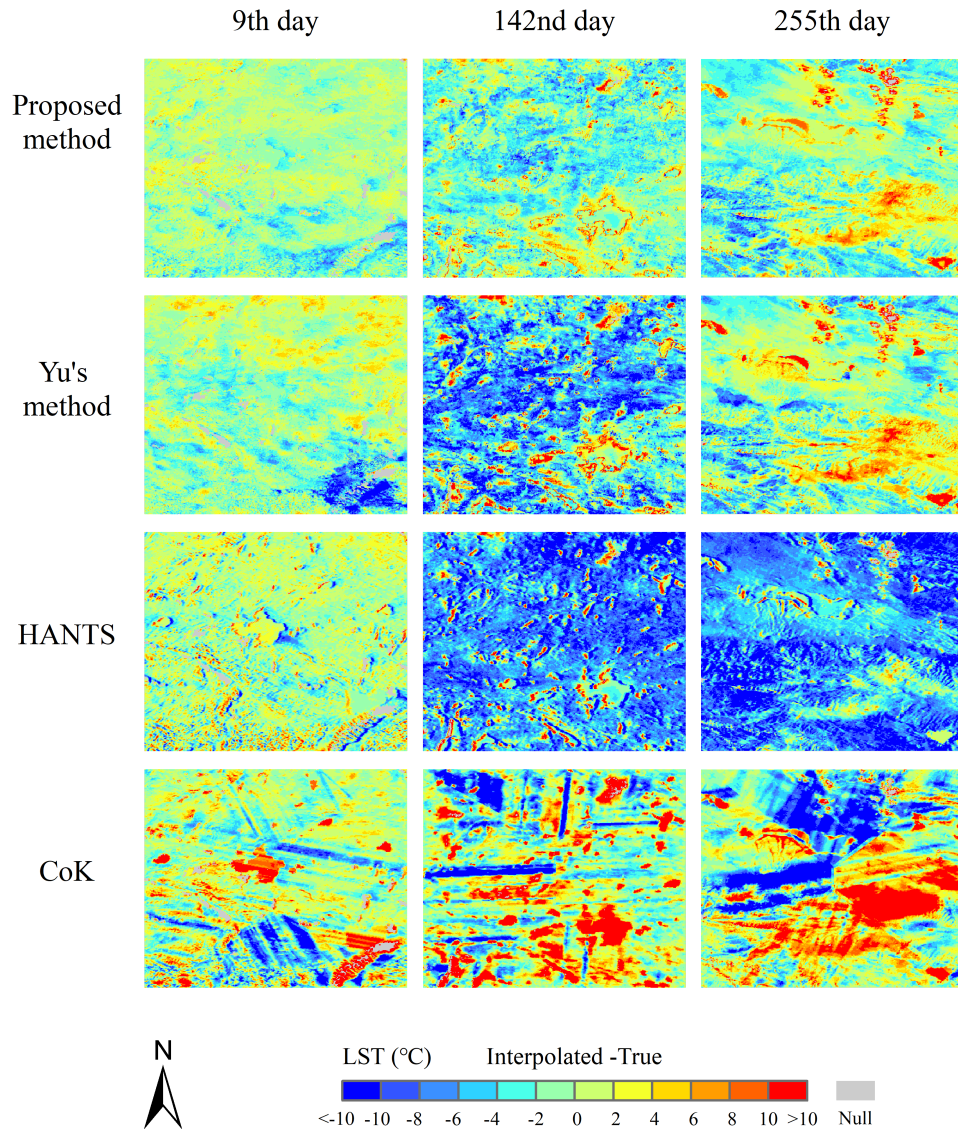


Fig. 6. Maps showing the differences between the interpolated daytime LST images and the preremoval true data in the fabricated data void experiment. Shown are the extents of the fabricated patches on the QTP. The columns are the different days of 2010. The rows indicate interpolation methods.

surface temperature over the Qinghai Lake, which is the biggest saltwater lake in China, is prone to be warmer than its land surroundings in winter and colder in summer due to the differences in specific heat between water and soils. In the winter image (see Fig. 3), surface temperatures happened to be missing over the lake area. The three methods succeeded in capturing winter characteristics over the lake, while the CoK [see Fig. 3(e)] failed. For HANTS, it reconstructed all information so that the valid values were also modified. It would cause obvious problems on some occasions. As shown in Fig. 4(d), summer temperatures over the Qaidam basin (marked with rectangles) would be much warmer than adjacent regions on the QTP due to much lower elevations in the basin. HANTS failed to describe this contrast in the Qaidam basin although it was able to explain a broad pattern of temperature distribution across the entire plateau. It is attributed to the fitting process used in HANTS, which is inadequate in recovering sudden changes in temperature [33].

The spatial patterns displayed on the two 2005 Terra LST images by the proposed approach and the Yu method were quite similar. To further examine their performance, we randomly selected 100 000 invalid pixels from the two images and compared their interpolated LST values by the two methods (see Fig. 5). Overall, the results obtained by the two methods were well correlated, with an SR of 0.88 on the winter nighttime image and 0.86 on the summer daytime image. The values of RMSE were 3.36 and 4.80 °C, and MAE 2.33 and 3.50 °C, respectively. The comparison simply indicates that despite the high spatial correlation they had, there were considerable discrepancies between the results yielded by the two methods.

#### B. Performance for the Fabricated Data Void Case

We plotted difference maps by subtracting the original values in the identified patches from the interpolated values as shown in Figs. 6 and 7. Warm colors denote overestimations made in

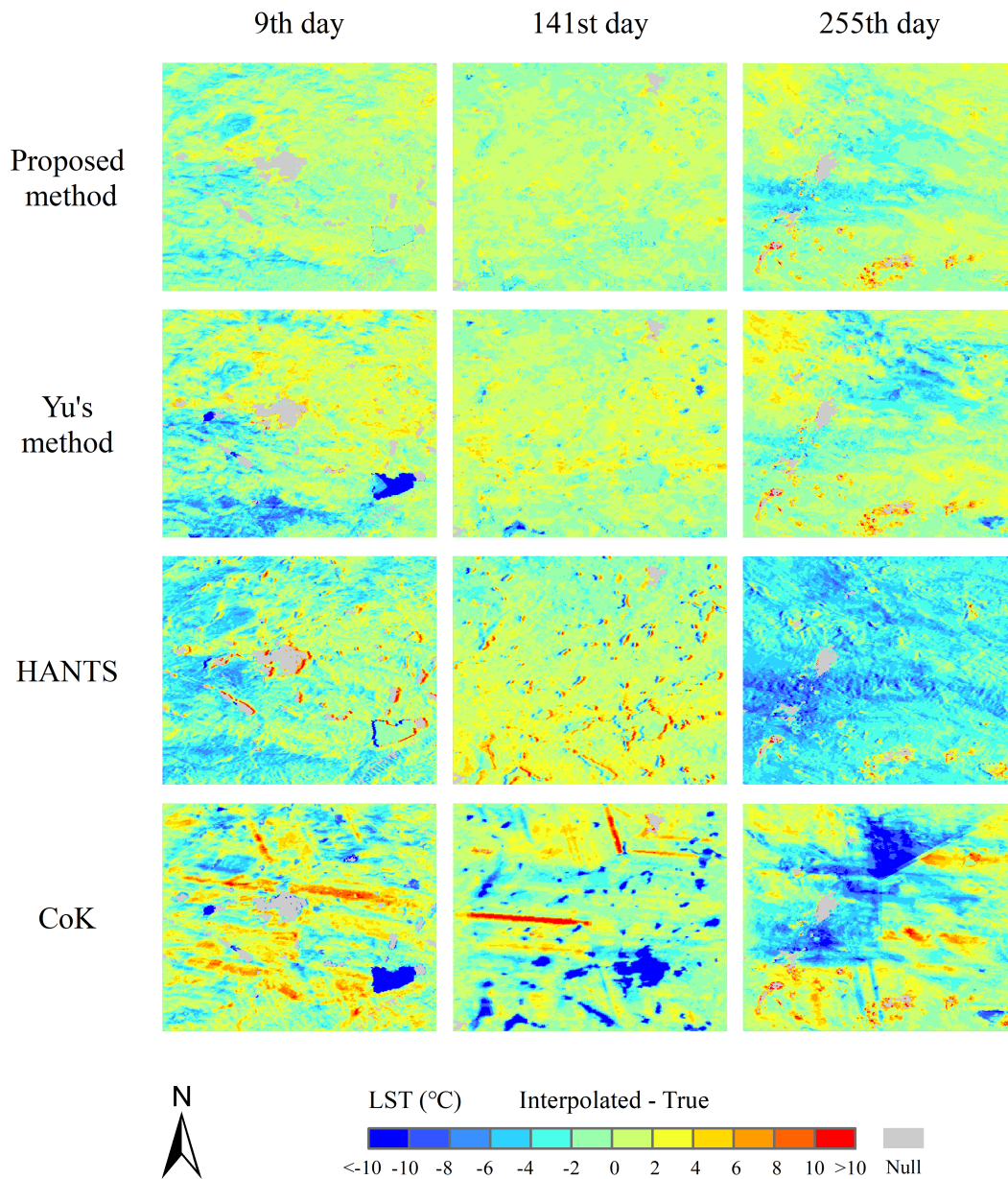


Fig. 7. Maps showing the differences between the interpolated nighttime LST images and the preremoval true data in the fabricated data void experiment. Same notations as Fig. 6 are applied.

the interpolation, whereas cool colors underestimations. The lower high-saturated colors on the difference maps, the better the performance of the investigated methods. In general, all methods yielded better results for the nighttime images (see Fig. 7) than the daytime images (see Fig. 6) as indicated by overall less high-saturated colors in Fig. 7. In the daytime cases (see Fig. 6), the proposed approach yielded the best interpolation results (row 1 of Fig. 6), whereas the CoK was unsurprisingly the worst, with plenty of strange geometries on the maps (row 4 of Fig. 6). While all methods consistently performed better on the ninth day of 2010 than other days, they varied considerably in interpolating the other two daytime images (142nd and 255th). In particular, HANTS seriously underestimated the LST values on the 142nd and 255th daytime images. So did the Yu method for the 142nd daytime image (see Fig. 6). In the nighttime cases (see

Fig. 7), by visual inspection, the proposed approach outmatched the peer methods, with light colors prevailing throughout those difference maps (row 1 of Fig. 7). The Yu method, although not as good as the proposed approach, also showed strength in interpolating large-area missing data (row 2 of Fig. 7). Conversely, HANTS and the CoK have given rise to considerable discrepancies in the nighttime results.

The quantitative metrics including SR, RMSE, MAE, and bias are shown in Fig. 8. It demonstrates the remarkable superiority of the proposed approach over the peer methods in interpolating clear-sky LST in terms of any metrics. For the proposed approach, the SR coefficients measured against the true data exceed 0.9 without exception, the highest among the others. The RMSE and the MAE were below 3.7 and 3.0 °C for daytime images, and both below 2.0 °C for nighttime images, respectively. The



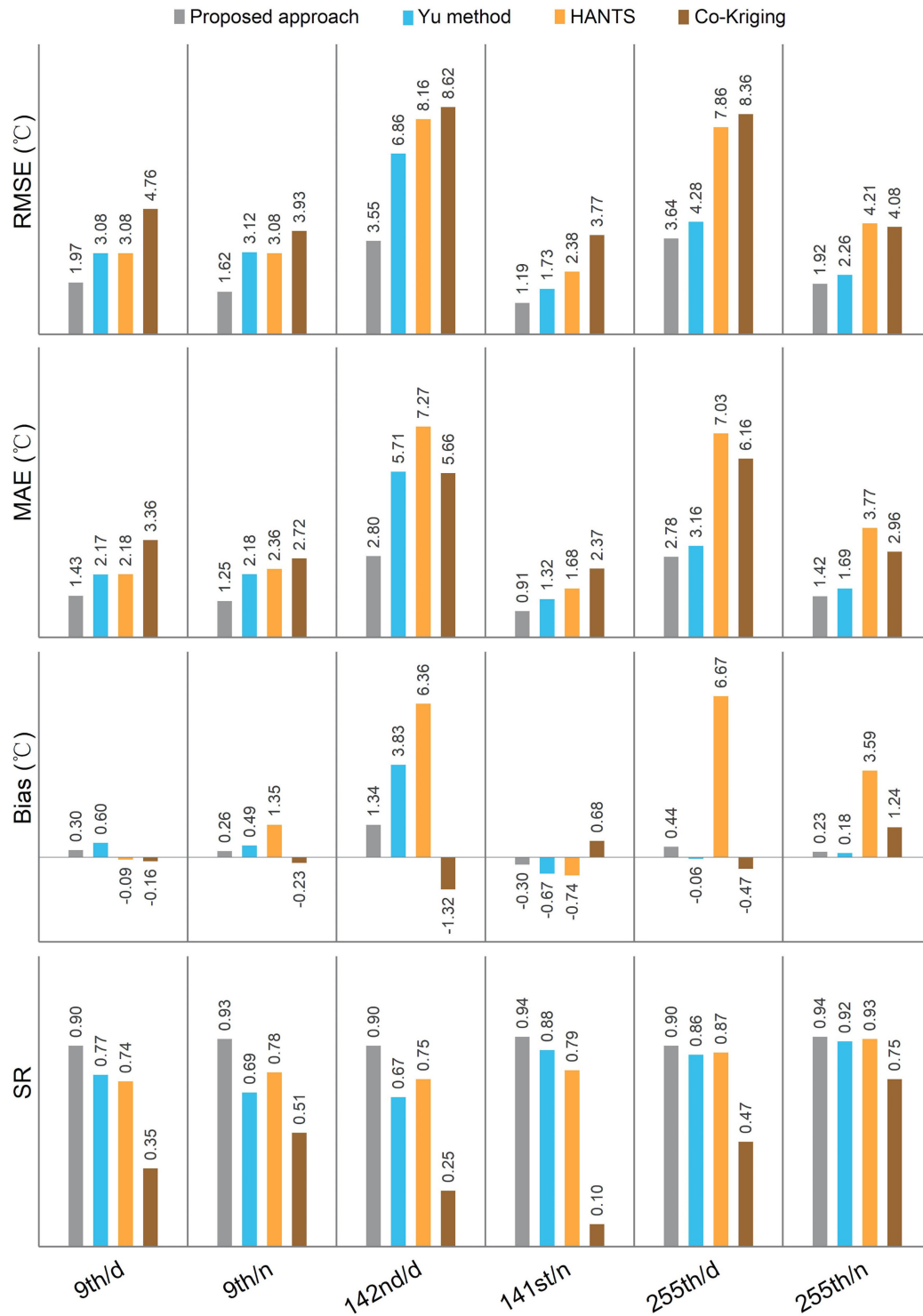


Fig. 8. Measured accuracies for the different methods applied to the selected LST images of 2010 on the QTP. RMSE: root mean square error; MAE: mean absolute error; and SR: spatial correlation coefficient. d: daytime; n: nighttime.

Yu method came next. The CoK was shown to have generally poorest performance with the lowest SR and largest RMSE values. When interpolating the daytime images, the RMSEs of the CoK exceeded 5.0°C, up to 8.0°C for the 142nd daytime image of 2010. HANTS is not good at interpolating large-area

missing data and often produced large RMSE, MAE, and bias, despite broadly acceptable SR values.

Both the proposed approach and the Yu method showed significant improvements over HANTS and the CoK in respect of evaluation metrics. The improvements are intimately related



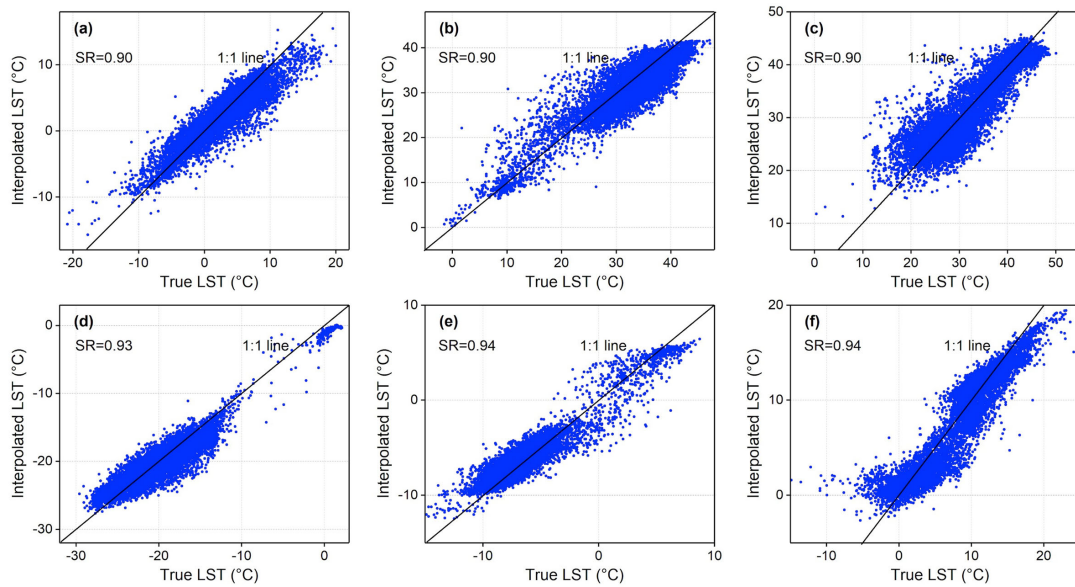


Fig. 9. Scatterplots of the results interpolated by the proposed approach versus the true data in the fabricated data void experiment. A random selection of 10,000 pixels from the LST images of 2010 were plotted. (a) the 9th day, (b) the 142nd day, (c) the 255th day, (d) the 9th night, (e) the 141st night, and (f) the 255th night.

to the use of both spatial and temporal information, instead of mere spatial or temporal information as used in CoK and HANTS, respectively. The Yu method also yielded favorable SR values ranging from 0.67 to 0.92, and small RMSEs ( $<3.2^{\circ}\text{C}$ ) for nighttime images. However, when dealing with daytime images, the Yu method is likely to induce large biases. For example, the RMSE was  $6.9^{\circ}\text{C}$  for the 142nd daytime image of 2010 (see Fig. 6). The daytime LST values are affected by more factors than the nighttime LSTs, and therefore, are hard to be accurately interpolated. The compromising performance of the Yu method is highly related to the large time gap between the interpolated image and the reference image used. As listed in Table I, the global reference image for interpolating the 142nd daytime image is the 212th daytime image, with a time interval as long as 70 days. The weakness of the Yu method, as demonstrated in this example, has been successfully overcome by the proposed method. The proposed approach reduced the RMSE value by about  $3.3^{\circ}\text{C}$  for the 142nd daytime image.

We further investigated the performance of the proposed approach on a pixel level. The interpolated results of a random selection of 10,000 invalid pixels from those 2010 Terra LST images are shown in Fig. 9. The interpolated results were generally more accurate for nighttime images than daytime images. The plots for the three nighttime images [see Fig. 9(d)–(f)] and cold-season daytime image [see Fig. 9(a)] were close to the 1:1 line, indicating that particularly better agreements can be achieved by the proposed approach for the nighttime images and cold-season images. The SR coefficients for nighttime images were consistently higher than daytime images. Nighttime LSTs and cold-season daytime LSTs are subject to less influencing variables than warm-season daytime LSTs. Therefore, both the proposed approach and the Yu method are able to work better for those specific timings.

### C. Improvement by Data Fusing

The improvements of using data fusion over individual initial estimates made by the DINEOF are shown in Fig. 10, where in almost all cases, the metric accuracies for the fused results were obviously improved. It proves the effectiveness of the use of data fusion in improving interpolation accuracies. The accuracies of the initial estimates varied by image. Most of them had comparable accuracies but some might considerably differ from the others. For example, the fourth initial estimate for the ninth daytime image of 2010 seriously deviated from the other three initial estimates and had an even slightly better agreement with the true data than the fused LST estimate in terms of SR. By examining the original data in the fabricated patch, abrupt temperature changes had occurred over the span across the two view times of the ninth daytime image and the reference image that the fourth estimate is associated with. As an initial estimate highly relies on the known values on the reference image, abnormal temperature changes on the reference image inevitably result in an unreliable estimate. A probability-based data fusion approach as adopted in the proposed approach can efficiently reduce the risk of introducing unexpected biases to the results, for which simple algebraic mean will never succeed.

The improved accuracies through data fusion differ over image timings. The daytime images generally had a lower accuracy for initial estimates than the nighttime images. Their improvements by data fusion were more obvious. The largest reductions in RMSE after data fusion amounted to 1.2, 1.34, and  $1.1^{\circ}\text{C}$  for the 9th, 142nd, and 255th daytime images, respectively. For the nighttime images, the fused results were also superior to the initial estimates with moderately better metric values. Reductions of about  $0.66^{\circ}\text{C}$  in both RMSE and MAE were obtained by imposing data fusion upon the initial estimates (see Fig. 10).

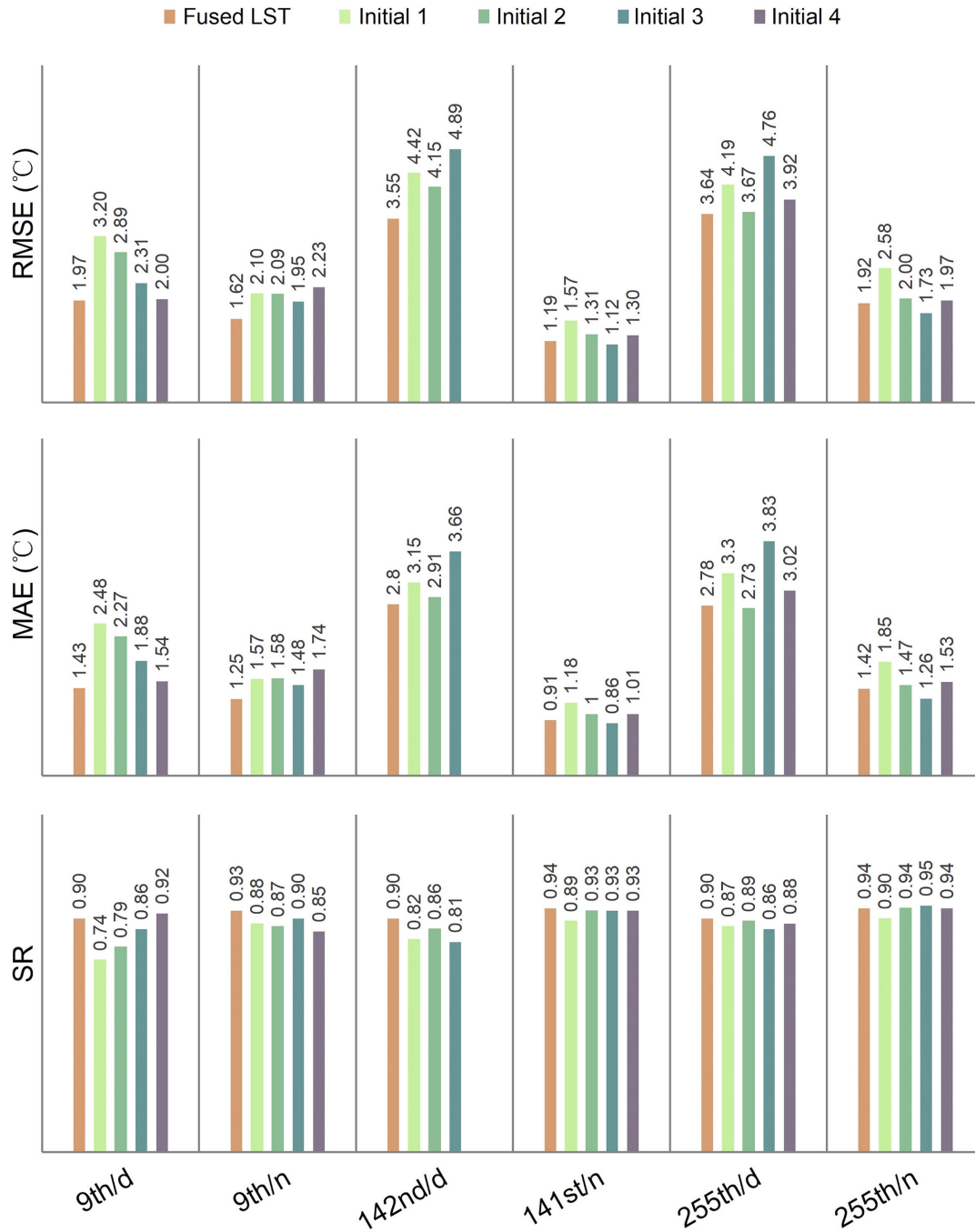


Fig. 10. Accuracy improvements of using data fusion over individual initial estimates for some exemplified LST images of 2010. Initials 1 to 4 are the first to fourth DINEOF initial estimates corresponding to four proximate reference images. Fused LST indicates the best estimate after fusing all initial estimates by a Bayesian data fusion approach. RMSE: root mean square error; MAE: mean absolute error; and SR: spatial correlation coefficient. d: daytime; and n: nighttime.

#### IV. CONCLUSION AND PROSPECTIVE

An improved approach for interpolating clear-sky MODIS LST in areas that suffer extensive data losses has been proposed. This approach extends prior work by using multiple temporal proximate images as reference images and introducing a Bayesian approach to find a best estimate based on multiple initial estimates made on the basis of multiple reference images through an EOF method. By those techniques, the weakness relating to using global reference images as used in the prior

work has been overcome and the interpolation accuracy has been significantly improved via the use of data fusion. The proposed method has proven to be effective in interpolating clear-sky equivalent LST with favorable accuracy in the presence of extensive spatial and temporal data losses through two experiments, one representing the real data void case and the other using fictitious data voids, based on the 2005 and 2010 Terra LST images on the QTP. Both experiments demonstrate that the proposed approach is much superior in interpolating large-area missing data than three established methods, i.e., the Yu method,

the HANTS model, and the co-kriging method with DEM as a variant. The interpolated results obtained by the proposed approach agreed well with the true data in the fictitious-void experiment, with high spatial correlation coefficients exceeding 0.9. The RMSE and mean absolute errors were less than 3.7 and 3.0 °C, respectively, for daytime images, and both less than 2.0 °C, for nighttime images. The combined use of multiple temporally proximate LST images as reference images and subsequent fusing of multiple initial estimates are important for improving interpolation accuracy.

In this study, we selected several auxiliary variables (such as DEM, NDVI, and solar radiation) as main factors influencing the characteristics of temporal changes in LST, which are critical for determining the similar pixel set. The influencing factors may vary region by region. Therefore, in practice, it is advised to determine the influencing factors according to regional characteristics. Despite that, in this study the MODIS/Terra LST data on the QTP were used as a demonstration; the proposed approach is theoretically applicable to the Aqua LST data and other variables in any large areas suffering similar extensive data losses. It should be stressed that the approach interpolates clear-sky equivalent LST values rather than real cloudy-sky values. This work provides an important step in the stepwise approaches toward fully recovering the LSTs affected by clouds.

## REFERENCES

- [1] P. Dash, F. M. Göttsche, F. S. Olesen, and H. Fischer, "Land surface temperature and emissivity estimation from passive sensor data: Theory and practice-current trends," *Int. J. Remote Sens.*, vol. 23, no. 13, pp. 2563–2594, Jul. 2002.
- [2] Z. Li *et al.*, "Satellite-derived land surface temperature: Current status and perspectives," *Remote Sens. Environ.*, vol. 131, pp. 14–37, Apr. 2013.
- [3] W. Kustas and M. Anderson, "Advances in thermal infrared remote sensing for land surface modeling," *Agricultural Forest Meteorol.*, vol. 149, no. 12, pp. 2071–2081, Dec. 2009.
- [4] Z. Wan, Y. Zhang, Q. Zhang, and Z. L. Li, "Quality assessment and validation of the MODIS global land surface temperature," *Int. J. Remote Sens.*, vol. 25, no. 1, pp. 261–274, Jan. 2004.
- [5] Z. Wan, "New refinements and validation of the MODIS land-surface temperature/emissivity products," *Remote Sens. Environ.*, vol. 112, no. 1, pp. 59–74, Jan. 2008.
- [6] H. Shen *et al.*, "Missing information reconstruction of remote sensing data: A technical review," *IEEE Geosci. Remote Sens. Mag.*, vol. 3, no. 3, pp. 61–85, Sep. 2015.
- [7] W. Yu, Z. Nan, Z. Wang, H. Chen, T. Wu, and L. Zhao, "An effective interpolation method for MODIS land surface temperature on the Qinghai-Tibet Plateau," *IEEE J. Sel. Top. Appl. Earth Observ. Remote Sens.*, vol. 8, no. 9, pp. 4539–4550, Sep. 2015.
- [8] H. Zhang, F. Zhang, G. Zhang, X. He, and L. Tian, "Evaluation of cloud effects on air temperature estimation using MODIS LST based on ground measurements over the Tibetan Plateau," *Atmos. Chem. Phys.*, vol. 16, no. 21, pp. 13681–13696, Nov. 2016.
- [9] F. Aires, C. Prigent, W. B. Rossow, and M. Rothstein, "A new neural network approach including first guess for retrieval of atmospheric water vapor, cloud liquid water path, surface temperature, and emissivities over land from satellite microwave observations," *J. Geophys. Res., Atmos.*, vol. 106, no. D14, pp. 14887–14907, Jul. 2001.
- [10] S. Chen, X. Chen, W. Chen, Y. Su, and D. Li, "A simple retrieval method of land surface temperature from AMSR-E passive microwave data—A case study over Southern China during the strong snow disaster of 2008," *Int. J. Appl. Earth Obs.*, vol. 13, no. 1, pp. 140–151, Feb. 2011.
- [11] S. Duan, Z. Li, and P. Leng, "A framework for the retrieval of all-weather land surface temperature at a high spatial resolution from polar-orbiting thermal infrared and passive microwave data," *Remote Sens. Environ.*, vol. 195, pp. 107–117, Jun. 2017.
- [12] H. R. Shwetha and D. N. Kumar, "Prediction of land surface temperature under cloudy conditions using microwave remote sensing and ANN," *Aquatic Procedia*, vol. 4, pp. 1381–1388, Feb. 2015.
- [13] M. Jin, "Interpolation of surface radiative temperature measured from polar orbiting satellites to a diurnal cycle: 2. Cloudy-pixel treatment," *J. Geophys. Res., Atmos.*, vol. 105, no. D3, pp. 4061–4076, Feb. 2000.
- [14] M. Jin and R. E. Dickinson, "A generalized algorithm for retrieving cloudy sky skin temperature from satellite thermal infrared radiances," *J. Geophys. Res., Atmos.*, vol. 105, no. D22, pp. 27037–27047, Nov. 2000.
- [15] J. P. A. Martins *et al.*, "An all-weather land surface temperature product based on MSG/SEVIRI observations," *Remote Sens.*, vol. 11, no. 24, Dec. 2019, Art. no. 3044.
- [16] X. Zhang, J. Pang, and L. Li, "Estimation of land surface temperature under cloudy skies using combined diurnal solar radiation and surface temperature evolution," *Remote Sens.*, vol. 7, no. 1, pp. 905–921, Jan. 2015.
- [17] C. Zeng, D. Long, H. Shen, P. Wu, Y. Cui, and Y. Hong, "A two-step framework for reconstructing remotely sensed land surface temperatures contaminated by cloud," *ISPRS J. Photogramm.*, vol. 141, pp. 30–45, Jul. 2018.
- [18] W. Yu, J. Tan, M. Ma, X. Li, X. She, and Z. Song, "An effective similar-pixel reconstruction of the high-frequency cloud-covered areas of Southwest China," *Remote Sens.*, vol. 11, no. 3, Feb. 2019, Art. no. 336.
- [19] X. Zhang, C. Wang, H. Zhao, and Z. Lu, "Retrievals of all-weather daytime land surface temperature from FengYun-2D data," *Opt. Exp.*, vol. 25, no. 22, Oct. 2017, Art. no. 27210.
- [20] G. Yang, W. Sun, H. Shen, X. Meng, and J. Li, "An integrated method for reconstructing daily MODIS land surface temperature data," *IEEE J. Sel. Top. Appl. Earth Observ. Remote Sens.*, vol. 12, no. 3, pp. 1026–1040, Mar. 2019.
- [21] C. Prigent, W. B. Rossow, E. Matthews, and B. Marticorena, "Microwave radiometric signatures of different surface types in deserts," *J. Geophys. Res., Atmos.*, vol. 104, no. D10, pp. 12147–12158, May 1999.
- [22] C. Prigent, C. Jimenez, and F. Aires, "Toward 'all weather,' long record, and real-time land surface temperature retrievals from microwave satellite observations," *J. Geophys. Res., Atmos.*, vol. 121, no. 10, pp. 5699–5717, May 2016.
- [23] J. C. Jiménez Muñoz, J. A. Sobrino, C. Mattar, and Y. Malhi, "Spatial and temporal patterns of the recent warming of the Amazon forest," *J. Geophys. Res., Atmos.*, vol. 118, no. 11, pp. 5204–5215, Jun. 2013.
- [24] M. L. Imhoff, P. Zhang, R. E. Wolfe, and L. Bounoua, "Remote sensing of the urban heat island effect across biomes in the continental USA," *Remote Sens. Environ.*, vol. 114, no. 3, pp. 504–513, May 2010.
- [25] S. Hachem, M. Allard, and C. Duguay, "Using the MODIS land surface temperature product for mapping permafrost: An application to northern Québec and Labrador, Canada," *Permafrost Periglac.*, vol. 20, no. 4, pp. 407–416, Nov. 2009.
- [26] D. Zou *et al.*, "A new map of permafrost distribution on the Tibetan Plateau," *The Cryosphere*, vol. 11, no. 6, pp. 2527–2542, Nov. 2017.
- [27] S. Yang, D. Zhang, L. Sun, Y. Wang, and Y. Gao, "Assessing drought conditions in cloudy regions using reconstructed land surface temperature," *J. Meteorol. Res.*, vol. 34, no. 2, pp. 264–279, Apr. 2020.
- [28] B. Scarino *et al.*, "Retrieving clear-sky surface skin temperature for numerical weather prediction applications from geostationary satellite data," *Remote Sens.*, vol. 5, no. 1, pp. 342–366, Jan. 2013.
- [29] J. Lai *et al.*, "Identification of typical diurnal patterns for clear-sky climatology of surface urban heat islands," *Remote Sens. Environ.*, vol. 217, pp. 203–220, Nov. 2018.
- [30] L. Ke, X. Ding, and C. Song, "Reconstruction of time-series MODIS LST in Central Qinghai-Tibet Plateau using geostatistical approach," *IEEE Geosci. Remote Sci.*, vol. 10, no. 6, pp. 1602–1606, Nov. 2013.
- [31] M. Neteler, "Estimating daily land surface temperatures in mountainous environments by reconstructed MODIS LST Data," *Remote Sens.*, vol. 2, no. 1, pp. 333–351, Jan. 2010.
- [32] T. Pede and G. Mountrakis, "An empirical comparison of interpolation methods for MODIS 8-day land surface temperature composites across the conterminous United States," *ISPRS J. Photogramm.*, vol. 142, pp. 137–150, Aug. 2018.
- [33] Y. Xu and Y. Shen, "Reconstruction of the land surface temperature time series using harmonic analysis," *Comput. Geosci.*, vol. 61, pp. 126–132, Dec. 2013.
- [34] W. L. Crosson, M. Z. Al-Hamdan, S. N. J. Hemmings, and G. M. Wade, "A daily merged MODIS Aqua-Terra land surface temperature data set for the conterminous United States," *Remote Sens. Environ.*, vol. 119, pp. 315–324, Apr. 2012.



- [35] N. C. Coops, D. C. Duro, M. A. Wulder, and T. Han, "Estimating afternoon MODIS land surface temperatures (LST) based on morning MODIS overpass, location and elevation information," *Int. J. Remote Sens.*, vol. 28, no. 10, pp. 2391–2396, May 2007.
- [36] M. Metz, D. Rocchini, and M. Neteler, "Surface temperatures at the continental scale: Tracking changes with remote sensing at unprecedented detail," *Remote Sens.*, vol. 6, no. 5, pp. 3822–3840, May 2014.
- [37] Z. Liu, P. Wu, S. Duan, W. Zhan, X. Ma, and Y. Wu, "Spatiotemporal reconstruction of land surface temperature derived from FengYun geostationary satellite data," *IEEE J. Sel. Top. Appl. Earth Observ. Remote Sens.*, vol. 10, no. 10, pp. 4531–4543, Oct. 2017.
- [38] E. Ozelkan, S. Bagis, E. C. Ozelkan, B. B. Ustundag, M. Yucel, and C. Ormeci, "Spatial interpolation of climatic variables using land surface temperature and modified inverse distance weighting," *Int. J. Remote Sens.*, vol. 36, no. 4, pp. 1000–1025, Feb. 2015.
- [39] S. Mukherjee, P. K. Joshi, and R. D. Garg, "Regression-kriging technique to downscale satellite-derived land surface temperature in heterogeneous agricultural landscape," *IEEE J. Sel. Top. Appl. Earth Observ. Remote Sens.*, vol. 8, pp. 1245–1250, Mar. 2015.
- [40] J. S. Yang, "Estimation of land surface temperature using spatial interpolation and satellite-derived surface emissivity," *J. Environ. Inform.*, vol. 4, no. 1, pp. 40–47, Sep. 2004.
- [41] X. Fan, H. Liu, G. Liu, and S. Li, "Reconstruction of MODIS land-surface temperature in a flat terrain and fragmented landscape," *Int. J. Remote Sens.*, vol. 35, no. 23, pp. 7857–7877, Dec. 2014.
- [42] F. Aires, C. Prigent, and W. B. Rossow, "Temporal interpolation of global surface skin temperature diurnal cycle over land under clear and cloudy conditions," *J. Geophys. Res., Atmos.*, vol. 109, no. D4, Feb. 2004, Art. no. D04313.
- [43] A. K. Inamdar, A. French, S. Hook, G. Vaughan, and W. Luckett, "Land surface temperature retrieval at high spatial and temporal resolutions over the southwestern United States," *J. Geophys. Res., Atmos.*, vol. 113, no. D7, Apr. 2008, Art. no. D07107.
- [44] J. Zhou, L. Jia, and M. Menenti, "Reconstruction of global MODIS NDVI time series: Performance of harmonic analysis of time series (HANTS)," *Remote Sens. Environ.*, vol. 163, pp. 217–228, Jun. 2015.
- [45] J. M. Beckers and M. Rixen, "EOF calculations and data filling from incomplete oceanographic data sets," *J. Atmos. Ocean. Technol.*, vol. 20, no. 12, pp. 1836–1856, Dec. 2003.
- [46] A. Alvera-Azcárate, A. Barth, M. Rixen, and J. M. Beckers, "Reconstruction of incomplete oceanographic data sets using empirical orthogonal functions: Application to the Adriatic Sea surface temperature," *Ocean Model.*, vol. 9, no. 4, pp. 325–346, Aug. 2005.
- [47] M. Kumar, D. P. Garg, and R. A. Zachery, "A generalized approach for inconsistency detection in data fusion from multiple sensors," in *Proc. Amer. Control Conf.*, Minneapolis, MN, USA, 2006, pp. 2078–2083.
- [48] S. Kang, Y. Xu, Q. You, W. Flügel, N. Pepin, and T. Yao, "Review of climate and cryospheric change in the Tibetan Plateau," *Environ. Res. Lett.*, vol. 5, no. 1, Jan. 2010, Art. no. 015101.
- [49] T. Yao *et al.*, "Third Pole climate warming and cryosphere system changes," *World Meteorol. Orga. Bull.*, vol. 69, no. 1, pp. 38–44, 2020.
- [50] L. Kumer, A. K. Skidmore, and E. Knowles, "Modelling topographic variation in solar radiation in a GIS environment," *Int. J. Geographical Inf. Sci.*, vol. 11, no. 5, pp. 475–497, Jul. 1997.
- [51] G. J. Roerink, M. Menenti, and W. Verhoef, "Reconstructing cloudfree NDVI composites using Fourier analysis of time series," *Int. J. Remote Sens.*, vol. 21, no. 9, pp. 1911–1917, Jun. 2000.



**Yuhong Chen** received the B.S. degree from Guizhou University, Guiyang, China, in 2017, and the M.S. degree from the School of Geography Science, Nanjing Normal University, Nanjing, China, in 2020.

Her current research interests include quantitative remote sensing and environmental remote sensing.



**Zhuotong Nan** received the B.S. degree from Lanzhou University, Lanzhou, China, in 1998, and the Ph.D. degree from Cold and Arid Regions Environmental and Engineering Research Institute of Chinese Academy of Sciences (CAREERI/CAS), Lanzhou, China, in 2003.

From 2007 to 2009, he was a Postdoctoral Researcher with the University of Pittsburgh, Pittsburgh, PA, USA, and from 2003 to 2015, a Professor with CAREERI/CAS. He is currently a Professor with Nanjing Normal University, Nanjing, China. He has

authored or coauthored more than 100 peer-reviewed papers related to permafrost simulation. His research interests include permafrost modeling, cold region hydrology, and application of geographic information systems.

**Shuping Zhao** received the B.S. degree from Lanzhou University, Lanzhou, China, in 1998, and the M.Sc. and Ph.D. degrees from the Graduate School of the Chinese Academy of Sciences, Beijing, China, in 2008.

Her current research interests include soil mechanics of frozen ground and permafrost modeling.

**Yi Xu** received the B.S. degree from Hohai University, Nanjing, China, in 2006, and the Ph.D. degree from the University of Pittsburgh, Pittsburgh, PA, USA, in 2013.

From 2013 to 2015, he was an Engineer with Tetra Tech Inc., Pasadena, CA, USA. His research interests include hydrological number modeling and model development.